Pinning effect on the band gap modulation of crystalline Be$_x$Zn$_{1-x}$O ternary films grown on Al$_2$O$_3$ (0001)

Dae-Sung Park[†], James. J Mudd[†], Marc Walker[†], Djelloul Seghier[†,§], Aleksander Krupski[†], Nessa Fereshteh Saniee[†], Chel-Jong Choi[‡], Chang-Ju Youn[‡], Sean Robert Craig McMitchell[†], and Chris F. McConville[*,†]

[†]*Department of Physics, University of Warwick, Coventry CV4 7AL, United Kingdom*

[‡]*School of Semiconductor and Chemical Engineering, Chonbuk National University, Jeonju 561-756, South Korea*

ABSTRACT: We have investigated the influence of Be concentration on the microstructure of Be$_x$Zn$_{1-x}$O films (from $x = 0$ to 0.77), grown on Al$_2$O$_3$ (0001) substrates using radio-frequency co-sputtering. With increasing Be concentration, the Be$_x$Zn$_{1-x}$O (0002) X-ray diffraction peak shows a systematic shift from 33.86º to 39.39º, and optical spectroscopy shows a blue-shift of the band gap from 3.24 to beyond 4.62 eV towards the deep UV regime, indicating that Be atoms are incorporated into the host ZnO lattice. During the band gap modulation, structural variations (e.g. phase separation and compositional gradients of Be) in the films were observed along with a significant change in the mean grain size. X-ray photoelectron spectroscopy indicates higher concentrations of metallic Be states in films with smaller grain size. Correlation between these two observations indicates that Be segregates to near grain boundaries. A structural model is proposed through simulation, where an increase in grain growth driving force dominates over the Be particle pinning effect. This leads to further coalescence of grains, reactivation of grain growth, and the uniform distribution of Be composition in the Be$_x$Zn$_{1-x}$O ternary alloy films.

KEYWORDS: *Oxide alloys, Band gap engineering, Be$_x$Zn$_{1-x}$O, Grain growth, Heterostructures, Thin films*
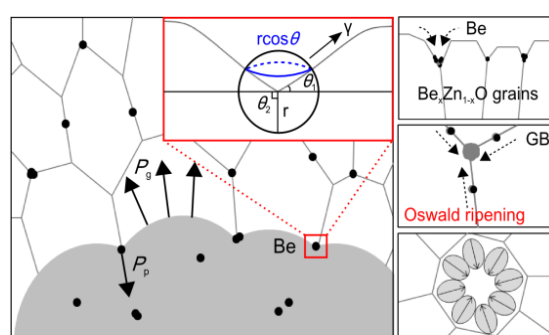
■ INTORDUCTION

Wide band-gap oxides have received a great deal of interest due to their potential use in optoelectronic applications, including ultraviolet (UV) laser diodes (LDs), light-emitting diodes (LEDs), high-mobility transistors and gas sensors.[1-6] Quantum confinement (QC) and the fractional quantum Hall effect (FQHE) are phenomena that have been observed in well-designed oxide heterostructures and can add to the wealth of potential applications.[7] In order to design such quantum structures, it is essential to understand the band-gap engineering of oxides and the nature of oxide-based heterointerfaces. In addition, various charge states can occur at such surfaces and interfaces (either charge accommodation or depletion), as a result of the surface termination, the formation of surface defects (e. g. oxygen vacancies or cation interstitials), the presence of impurities (e. g. hydrogen - H$_i$) or other chemisorbed species.[8-10]

ZnO-based materials have many applications and exhibit many interesting physical and electronic properties, including a large exciton binding energy (~ 60 meV) at room temperature, and high transparency in both ultra-violet (UV) and visible spectral ranges.[11] In a wider band-gap engineering process of

ZnO-based materials, A. Ohtomo *et al.*[12] first proposed that the band gap energy (E$_g$) of Zn$_{1-x}$Mg$_x$O could be tuned from 3.3 eV (ZnO) to 7.8 eV (MgO) by substitution of Mg into Zn lattice sites in the wurtzite structure. The alloying process, however, was limited to $x \leq 0.36$ to a structural transition from the ZnO hexagonal phase to the rocksalt phase of MgO at high concentration. Ryu *et al.*[13] suggested that the E$_g$ for ZnO could be fully modulated by alloying with BeO (E$_g$ = 10.6 eV) without a structural phase transition due to the two materials having the same hexagonal symmetry. Subsequently, a Be$_x$Zn$_{1-x}$O-based multi-quantum-well structure was designed by periodically stacking ZnO wells with Be$_{0.2}$Zn$_{0.8}$O barriers, resulting in UV light emission generated from a conventional LED structure.[5] After this demonstration, Klingshirn *et al.*[14] suggested that one possible explanation of compositional fluctuations and local segregation, was diffusion of Be to the ZnO interfaces in the quantum well device structures. Therefore, understanding the growth mechanisms of Be$_x$Zn$_{1-x}$O films on large-mismatched substrates is key to improving device performance. In previous studies, growth of Be$_x$Zn$_{1-x}$O ternary thin films using various growth methods[15-18] resulted in poor quality single crystals due to the

tetrahedral ionic radius of Be^{2+}(0.27 Å) being much smaller than that of Zn^{2+}(0.60 Å). This size difference can lead to a change in crystal space group from hexagonal ($P6_3mc$ and $Pmc2_1$) to other crystal symmetries (i.e., orthorhombic $Pmn2_1$ or $Pna2_1$) or zinc blende (F43m).[19] Thermodynamic instability can also occur as a miscibility gap for BeZnO alloy system, leading to compositional fluctuation or phase segregation.[20] Finally, considerable strain arises from the lattice mismatch between the alloy film and substrate. The interface normally favors a three-dimensional (3D) growth mode, resulting in a columnar structure, mixed growth orientations, and a rough surface morphology.[21,22] In this manuscript the influence of Be concentration on grain growth in crystalline $Be_xZn_{1-x}O$ thin films (from $x = 0$ to 0.77) has been investigated. It was found that a systematic change of the lattice parameter and optical band gap (E_g) occurs with increasing Be concentration, meanwhile non-uniform distribution of Be in the films was also observed for compositions ranging from $x = 0.16$ to 0.41. A particle pinning model has been developed to interpret the compositional fluctuations and segregation of Be, following coalescence of the smaller-sized grains in terms of grain boundary movement as a function of Be concentration.

■ RESULTS AND DISCUSSION

Film optical and structure properties. The change in the cut-off wavelength of the transmittance spectra for the $Be_xZn_{1-x}O$ alloy films as a function of Be fraction is shown in Figure 1a. The spectral range available (220-850 nm) was insufficient to measure for the films with high Be content due to the wider band gap energies. However, there was clearly a continuous shift of the spectra into the deep UV energy region and a high transparency of over 85 % as Be concentration increased. Based on these transmittance spectra, the absorption coefficients (α), of the films were evaluated from $T = A\exp(-\alpha d)$, where, T is the transmittance of the film, A is constant and d is the film thickness. Consequently, by taking a linear extrapolation of the leading edge of α^2 versus ($h\nu - E_g$), the optical band gap energies in the limit of the spectral region were determined to range from 3.24±0.01 to 4.62±0.06 eV for Be concentrations up to $x = 0.51$ (see the inset of Figure 1a).[23] Tailing of the absorption edge obtained was found as Be concentration increased. This is commonly associated with a decrease of the crystalline quality.[24,25] Changes in the optical band gap energies, taken from transmittance spectra, exhibited a non-linear dependence on the Be mole fraction (Figure 1b) due to a large bowing effect (b). The values of b were calculated to 4.8±0.2, 4.6±0.4, 6.0±0.3, 7.8±0.3, and 9.5±0.2 eV in the range of Be concentration from $x = 0.05$ to 0.51. The large bowing parameters, b, can be ascribed to the considerable difference of atomic size and large chemical mismatch between the Zn^{2+} and Be^{2+}. A large increase in bowing parameters was observed as the Be concentration increased. This could be associated with additional band repulsion between the O $2p$ and the Zn $3d$ orbitals in the electronic band structure of the Be-rich alloys, possibly resulting in a large band gap reduction.[19,26] Lattice strain effect on the redistribution of the density of states in hexagonal symmetry of the large-mismatched films also requires consideration. Consequently, the optical results confirm that the band gap of ZnO can be tuned by incorporating Be into the host lattice although some structural deterioration should be expected. However, it is noted that the calculated optical values might be overestimated due to a

spectral merging effect, which embedded the local distribution of Be composition in the optical spectroscopy measurement.
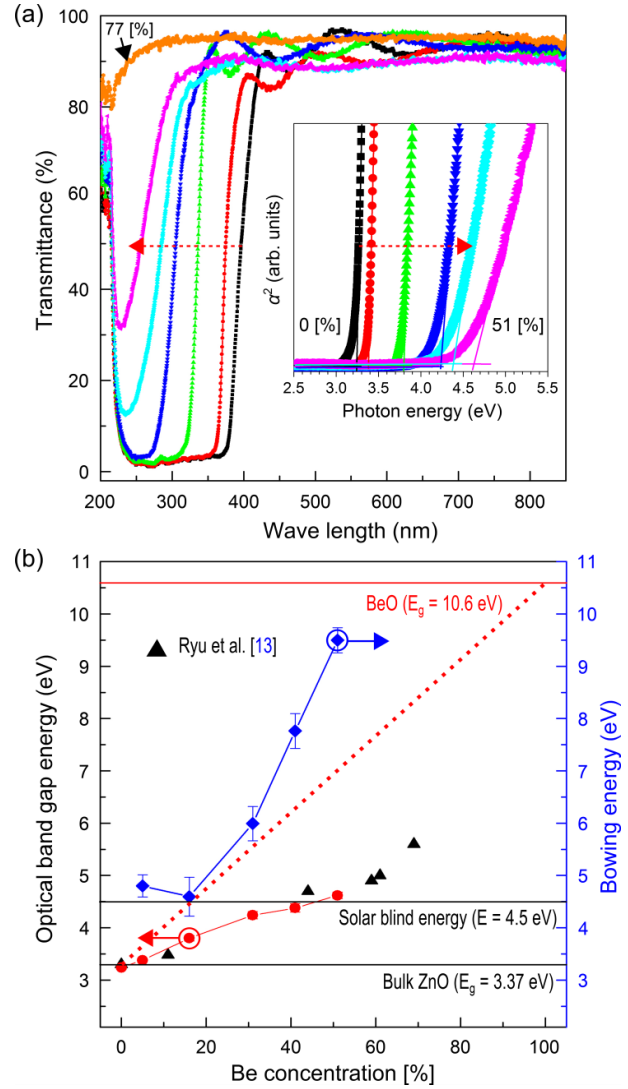

Figure 1. (a) Transmittance spectra of the $Be_xZn_{1-x}O$ films with an increase in Be concentration [%] from $x = 0$ to 0.77, (inset of (a)) the curve of α^2 vs photon energy ($h\nu - E_g$) for the films composed by $x = 0$ - 0.51 and (b) a comparison in band gap energies with the previous report with bowing parameters, b, for the $Be_xZn_{1-x}O$ alloys.

X-ray diffraction (XRD) patterns of the $Be_xZn_{1-x}O$ thin films grown on (0001) Al_2O_3 substrate, taken in the θ-2θ geometry are shown in Figure 2a. All films were shown to be preferentially oriented along the c-axis plane (0001) of wurtzite phase. In addition, the (10-10) and (10-11) growth orientations were also observed. There was a significant shift in the (0002) diffraction peak position as Be concentration increased. This suggests a structural change from the undoped ZnO structure (33.9°) towards a hexagonal BeO-type structure (41.1°). From this shift, a decrease in c-axis lattice parameter was deduced from 5.23 for to 4.80 Å as shown in Figure 2b, confirming the lattice compression required for incorporating Be^{2+} into ZnO. Calculations based on *Vegard*'s law confirmed the Be fraction

in the alloy films as $x = 0.05$, 0.16, 0.31, 0.41, 0.51, and 0.77.[27] This revealed that Be atoms were well-substituted into Zn sites and that the c-axis hexagonal structure was thus primarily maintained in all films. Broadening of the (0002) diffracted peak was also observed as Be composition gradually increased, suggesting the deterioration of film crystal quality. This is also indicative of a reduction of crystallite size with increasing Be content in the alloy films. It is known that adatom diffusion on a surface to islands can be kinetically restricted by strain concentration near step edges during island growth. Since the strain-induced energy barrier to adatom movement at the island edge is proportional to lattice mismatch, smaller coherent

Figure 2. (a) XRD θ-2θ scans of the Be$_x$Zn$_{1-x}$O films as a function of Be concentration [%], and abnormal peaks appearing between (10-10) and (0002) Be$_x$Zn$_{1-x}$O plane reflections are signified by blue-triangles. (b) The XRD (0002) peak positions in 2θ and c-axis lattice parameters as a function of Be content [%].

islands can be formed in higher lattice-mismatch system.[28] Substantial elastic strain generated from lattice mismatch between the Be$_x$Zn$_{1-x}$O films from lattice mismatch between the Be$_x$Zn$_{1-x}$O films and the substrate would be further increased with the addition of more Be. This is due to the smaller atomic size of Be and causes smaller crystallites as the excess strain is relaxed. Hence, large lattice mismatch (more than 18%) at the Be$_x$Zn$_{1-x}$O film/substrate interface is assumed to initiate a three-dimensional (3D) grain growth to minimize the total energy configuration (strain energy + surface energy). This leads to the formation of smaller crystallites and also misaligned (tilted/twisted) domains with random orientations.[29,30] As a result, these growth features with smaller grains are induced by increased lattice mismatch strain. Furthermore, since grain growth in films is driven by a reduction of total energy at grain boundaries, the grain boundary migration for the film grain growth could play a crucial role in the formation of crystalline Be$_x$Zn$_{1-x}$O films. This point will be discussed in more detail later. In the Be concentration range from $x = 0.16$ to 0.41, asymmetrically split (0002) peaks and extra peaks between the (10-10) and (0002) orientations, in Figure 1a, were clearly observed. Those two distinct peaks shift towards each other as Be concentration increases and merge to form a single peak by a concentration of $x = 0.51$. The peak then reduced in intensity and, disappeared at the highest Be concentration of $x = 0.77$, where only an hexagonal (0002) peak was seen. Structural fluctuations may be attributed to a non-uniform distribution of Be atoms and a higher level of lattice stress from grain boundaries and the substrate interface during film growth.[20,31] In previous theoretical studies, such a phase separation in the Be$_x$Zn$_{1-x}$O alloy system was expected due to a large enthalpy of its formation arising from large mismatch between ZnO and BeO. Imbalance in diffusivities between the solute (Be) and solvent (ZnO) in different grain growth orientations driven by the reduction in surface energy could also be the cause of variation in Be composition.

Film surface morphology and chemical composition. AFM topography images (10×10 μm^2) of the Be$_x$Zn$_{1-x}$O films grown on (0001) Al$_2$O$_3$ substrates are shown in Figure 3a. The images indicate that all film microstructures are consisted of grains, corresponding to a three-dimensional (3D) columnar growth mode. Various sizes of grains were randomly distributed on the film surfaces up to Be fraction of $x = 0.51$. For Be concentration of $x = 0.77$, a smaller grain size became dominant as shown in a 1×1 μm^2 scan of the Be$_{0.77}$Zn$_{0.23}$O film (right-bottom image in Figure 3a). The distribution of different grain sizes on film surface is consistent with XRD measurements, which indicated a coexistence of different growth orientations and broadening of the (0002) diffraction peak.[30] The average grain size for the films were found to decrease from ~ 68.6nm for the $x = 0$ to ~ 27.8 nm at $x = 0.31$. An increase of grain size followed at higher values of x to ~ 76.0 nm at $x = 0.77$. It should be noted that the average grain size obtained from AFM analysis differed from that obtained from XRD (using *Debye-Scherrer* formula), as depicted in Figure 3c.[32] Further insight into this can be obtained by analysis of the AFM phase image (Figure 3b). It was found that the average grain size appeared bigger due to a set of fine-grains along grain boundaries combining as Be concentration increased from $x = 0.31$ to 0.77. This is shown by spectral images of the
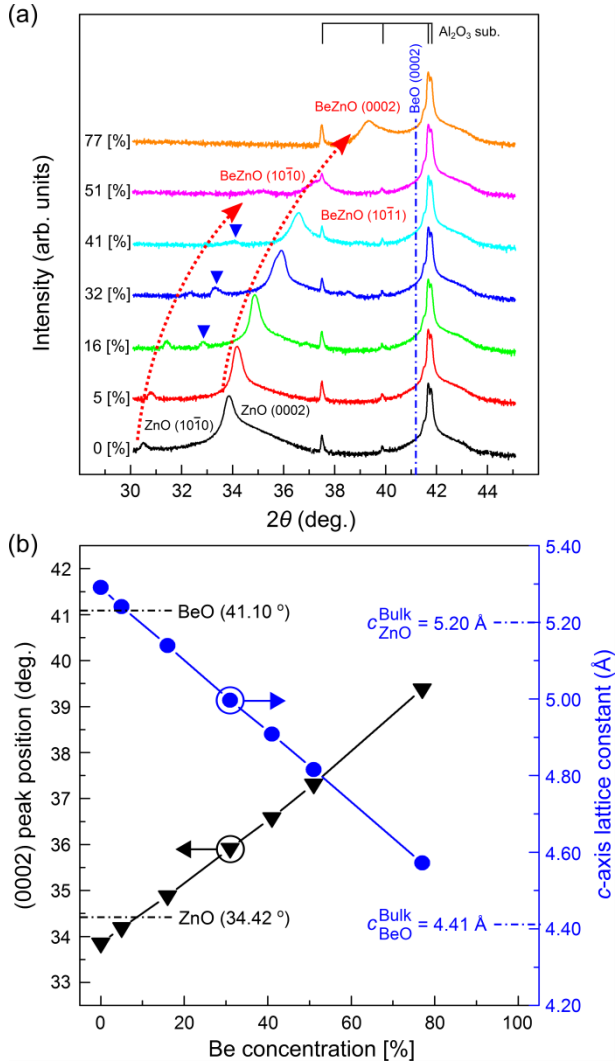
Figure 3. (a) AFM topography (10 × 10 μm²) images of the Be$_x$Zn$_{1-x}$O films for x = 0, 0.5, 0.31, 0.51, and 0.77, and the (1 × 1 μm²) image of the Be$_{0.77}$Zn$_{0.23}$O film. (b) Phase (1 × 1 μm²) images of the selected Be$_x$Zn$_{1-x}$O films composed by Be concentration, x = 0.31, 0.51, and 0.77, magnified spectrum images (right-top and -bottom) for selected areas -A and -B of x = 0.51 and 0.77, respectively. (c) The profile of crystallite size (based on FWHM values of the XRD (0002) diffraction peaks for the films) and average grain sizes (AFM) as a function of Be concentration.

selected grains (A and B). It reveals that the formation of the bigger grain size is a consequence of coarsening the fine-grains in the grain boundary junctions.

The XPS spectra of Be 1s and Zn 3p core-levels for the Be$_x$Zn$_{1-x}$O films composed by different Be contents are shown in Figure 4a. Spin-orbit splitting of Zn 3p core-level of all films at the binding energy (BE) of around 89 eV was found into Zn 3$p_{1/2}$ (higher BE side) and Zn 3$p_{3/2}$ (lower BE side).[33] The Zn 3p core-level peak showed broadening and a shift to the higher BE region with increasing Be concentration in the films. This is attributed to Zn ions in different net-charge distribution in the wurtzite alloy coordination, the presence of a variety of surface species (e.g. surface hydroxylation on polar surface: Zn-O-H), and the increase of number of Zn ions in defect states.[34,35] These imply increased surface area to volume ratio on decreasing the crystallite size and non-stoichiometric wurtzite environment as Be concentration rises. As seen in Figure 4b, the XPS spectrum for the undoped ZnO film showed a broad feature (100 to 120 eV) originating from screening effect of photo-excited electrons in surface plasmon excitation and inelastic collision processes (e. g. electron-electron and electron-phonon scatterings). This implies that the films surface possesses free-electron carriers due to native defects/unintentional impurities (e. g. V$_o$, Zn$_i$, and H$_i$) as is typical in undoped ZnO. It could also contribute to a surface band bending effect.[8,9,36] The relative intensity of the plasmon peak decreased continuously, revealing both the reduction of free-carriers and deterioration of crystallinity in terms of the number of photo-excited electrons in relatively long-pass distance on the films surface. So, the plasmon effect on the Be$_x$Zn$_{1-x}$O film surfaces at high Be content in Be 1s core-level is negligible, allowing the Be 1s core-level deconvoluted into two components at BEs of 111.2±0.05 and 114.4±0.05 eV, respectively (denoted in Figure 4b). Those two distinct components are associated with metallic Be (Be$_M$) and Be-O bond (Be$_O$) states on the surface.[37-39] Apparently, the peak intensity at BE of around 114 eV increased continuously, suggesting again well-incorporation of Be into the host, and is consistent with above XRD and optical spectroscopy measurement results. The highest ratio of Be$_M$ to Be$_O$ was observed at a Be concentration of x = 0.31. Then, a continuous decrease of the ratio was observed with further addition of Be up to x = 0.77. All fitting parameters and the relative percentages of Be$_M$ and Be$_O$ for the

Be 1s core level spectra found by evaluating the intensity region of Zn 2p, Be 1s, and O 1s core-levels for all Be$_x$Zn$_{1-x}$O films are presented in Table 1. Likewise, surface Be concentration was lower compared to the film bulk. A possible explanation is that this is caused by a surface segregation process through the removal of surface atoms to minimize surface energy.[34,40]
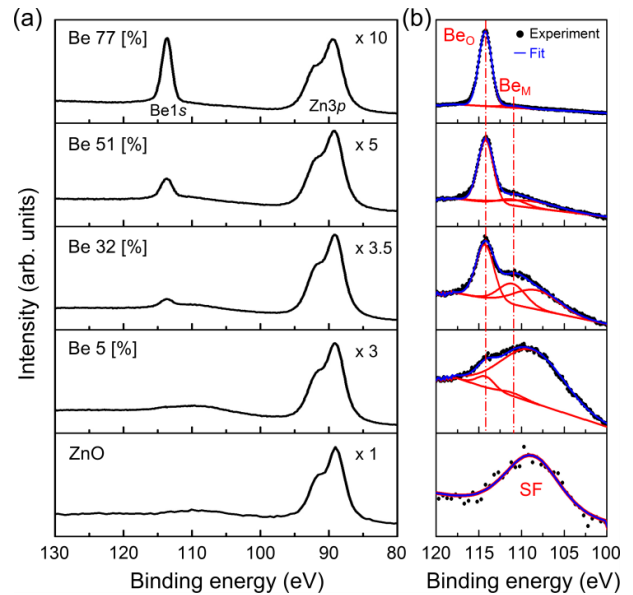

Figure 4. (a) Be 1s and Zn 2p XPS spectra for the ZnO and Be$_x$Zn$_{1-x}$O alloys as Be fraction, x, increases. (b) Experimental Be 1s core level spectra for all films are fitted into Be-O bonding (Be$_O$), metallic Be (Be$_M$), and surface plasmon (SF) components using a Shirley background with a linear component and Voigt (mixed Lorentzian-Gaussian) line shapes (solid lines).

Particle pinning model and discussion. From the above experimental observations, we suggest a mechanism for grain growth of crystalline Be$_x$Zn$_{1-x}$O on Al$_2$O$_3$ substrates. It was found that Be concentration in the alloy films significantly affects grain structure and its size. The model outlined below

Table 1. Parameters (binding energy, Lorentzian percentage of the Voigt line shape (*L*), and full width at half maximum (FWHM)) of Be 1*s* core level fitting and quantification values (%) of Be-O bonding (Be$_O$) and metallic Be bonding (Be$_M$), from XPS spectra (Al K$_\alpha$; hν = 1486.6 eV) for Be$_x$Zn$_{1-x}$O as a function of Be concentration [%]. The quantification analysis of atomic compositions (Zn, Be, and O) for all films was determined from the areas of the Zn 2*p*, Be 1*s*, and O 1*s*.

Sample	Bonding	Binding energy (eV)	L (%)	FWHM (eV)	Relative percentage (%)
Be 5 [%]	Be$_O$	114.2±0.03	8	2.2	6.67±0.3
	Be$_M$	111.2±0.03	8	3.2	2.74±0.2
Be 31 [%]	Be$_O$	114.4±0.03	8	2.3	22.95±0.5
	Be$_M$	111.2±0.03	8	3.7	13.02±0.3
Be 51 [%]	Be$_O$	114.2±0.03	8	2.1	34.42±0.5
	Be$_M$	111.0±0.03	8	3.7	5.94±0.4
Be 77 [%]	Be$_O$	114.3±0.03	8	1.8	44.68±0.3
	Be$_M$	111.1±0.03	8	3.0	1.82±0.2

describes a grain boundary drag effect by Be particles at grain boundaries, leading to the formation of smaller sized grain during growth as illustrated in Figure 5a. It is common in grain growth that the grain size depends on migration of the grain boundaries arising from the difference of grain curvatures (pressure; P_g) owing to chemical potential difference ($\Delta\mu$) described by [29,41,42]

$$\Delta\mu = \frac{2\gamma}{D} = p_g$$
(1)

where, γ, and D are interfacial energy at the boundary and mean grain size, respectively. The matrix grain boundary mobility is interrupted by pinning of solute particles, occupied at grain boundary areas.[43] Namely, pinning particles at grain boundaries areas reduces the Gibbs free energy, retarding the movement of the matrix grain boundaries during growth. The grain boundary attached to pinning particles along $2\pi r\cos\theta_1$, where, r is the radius of particle, is illustrated in Figure 5a. The maximum pining pressure (P_p) of the particles can be denoted by

$$p_p = \frac{3f}{2\pi r^2} \cdot (2\pi r\cos\theta_1 \gamma)\sin\theta_2 \approx \frac{3f\gamma}{2r}$$
(2)

where, f is volume fraction of the particles in the unit area of a random plane. The first term is the mean number of the particles intersecting the unit area of a random plane, and the second term is the maximum particle pinning force with a drag angle of $\theta_1 = 45°$ and a surface pulling angle of $\theta_2 = 90°$ at grain boundary. As above the two driving pressures counterbalance each other, and the pinned grain size, D_{max}, is approximately determined by

$$D_{max} = \frac{4r}{3f}$$
(3)

According to this model, metallic Be particles may favor lower energy sites at grain boundaries rather than matrix of the grain, subsequently inhibiting the grain boundary mobility. As a result, reduction of grain size occurs as shown in Figure 5b.
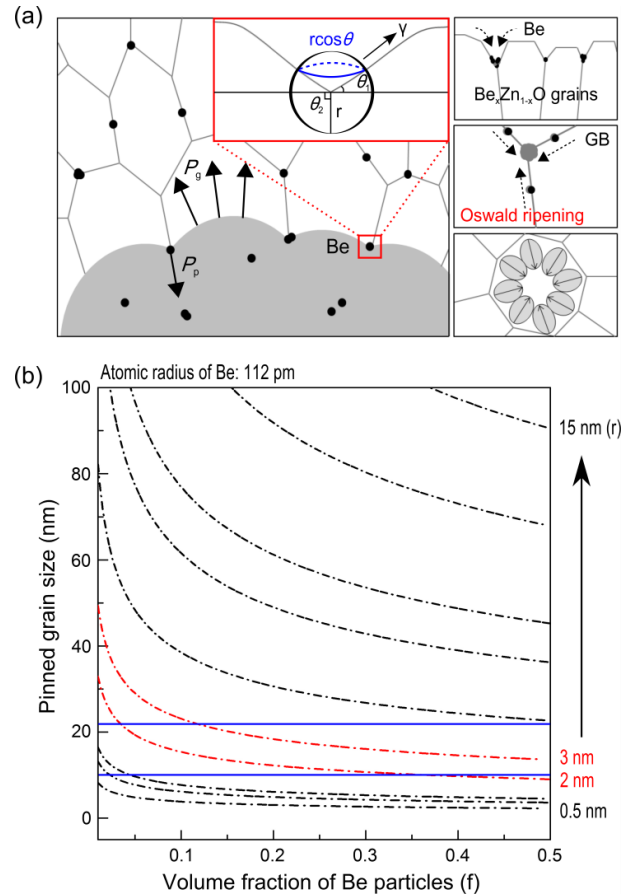

Figure 5. (a) Schematic diagrams for grain growth model for crystalline Be$_x$Zn$_{1-x}$O pinned by Be particles,[29] and (b) pinned grain size (D_p) as a function of volume fraction (*f*) of Be pinning particles, for values of the Be particle radius (*r*) from 0.5 to 15 nm. The region between the two blue-lines represents the pinned grain size range with Be particle size of 2 - 3 nm, which is consistent with the experimental results.

In a similar case, B. Ingham *et al.* reported that metallic Al atoms at grain boundaries restrict ZnO grain growth in the formation of spinel crystallites as $ZnAl_2O_3$.[44] Our AFM and XPS results showed a mean grain size that was inversely proportional to the amount of metallic Be on all film surfaces. Furthermore, one can expect that increasing Be content in the films contributed to increasing the volume fraction of Be particles at grain boundaries and thus a decrease in grain size. There is, however, an inconsistency in crystallite size and mean grain size measured by XRD and AFM. This discrepancy can be reconciled by considering the change of the Be pinning pressure at the grain boundaries with the increase of Be pining particle size. An Ostwald ripening process for Be particles occurs through grain boundary slabs, resulting in a coarsening of the particles bigger and in turn decreasing the pinning pressure, P_p.[45] When the driving pressure of the grain growth is sufficient to overcome pinning pressure of Be particles at grain boundary, the movement of grain boundary in the main grain growth restarts as part of the coalescence process. Interestingly, a two-step coalescence process in different grain boundary configurations was exhibited at a Be concentration of $x = 0.77$. Initially, the fine-sized grains are coarsened to concave inward under the formation of an eight-junction grain boundary that minimizes interface energy between the grains. Then, a set of the coarsened fine-grains combines in a triple-junction boundary favoring a distinct grain growth direction in an abnormal grain growth mode. At the same time, Be particles could encounter lattice matrix grains due to the Be concentration gradient driving mass transport. Eventually, Be concentration is uniformly distributed across the fine grains via the grain boundary junctions and metallic Be states are reduced as shown in XPS result.

The approximate size of Be pinning particles depends on the volume fraction of the particles and the pinned grain size as depicted in Figure 5b. Zener *et al.* first proposed the particle pinning model with a random distribution of second phase particles at boundary intersections, i.e. the volume fraction, f [1], of the particles represents a random dispersion in both the planar (2D) and volume (3D) cases.[43] In our model construction, since Be pinning particles are mostly placed at grain boundary areas rather than in the $Be_xZn_{1-x}O$ matrix grains, the model has been modified by requiring a non-random distribution of Be particles in a 3D system. Hillert *et al.* also suggested an applicable pinning model in a 3D volume fraction of particles with modified parameters as given by [46]

$$\widetilde{D}_{max} = \frac{3.6r}{3f^{0.33}}$$

(4)

where, $\widetilde{D}_{max}$ is the pinned maximum grain size in a 3D system. The equation is only valid for $f > 0.1$ (10 %) as the proportion of metallic Be on the $Be_{0.31}Zn_{0.69}O$ film surface was approximately 13 % as measured by XPS. As a result, the simulated plots (denoted by red dot-dashed line in Figure 5b) of pinned grain sizes with Be particle size of 2 - 3 nm are in good agreement, found from AFM results. Note that in this approximation of pinned grain sizes including Be particles, several plausible interactions (e. g. Be particle drag, Be solute precipitation, and re-dissolution) between grain boundaries and the Be solute have been considered.

Another aspect of this study is a coupling between pinned grain size pinned by Be particles at grain boundaries and the resulting surface variation on the films, plays a significant role in the compositional fluctuation of Be and the grain boundary areas. As the $Be_xZn_{1-x}O$ grain matrix is encountered by Be particles, the surface curvature of the matrix grain gives rise to the distribution of local Be concentration. In addition, an increased grain boundary area in the films promotes an increase in effective surface areas (higher surface-to-volume ratio), encouraging surface chemisorptions, e. g. oxygen chemisorption. These results in the formation of charge trapping/scattering centers, and thus potential barriers for charge transport.[47,48] Therefore, the variation in the surface properties during grain growth is a matter of concern as it may cause substantial non-uniformity in film properties and make applications of $Be_xZn_{1-x}O$ quantum structures or, indeed, other heterostructures problematic.

■ CONCLUSIONS

Crystalline $Be_xZn_{1-x}O$ films ($0 \leq x \leq 0.77$) have been grown on *c*-axis Al_2O_3 substrates by RF co-sputtering. Our experimental investigations clearly confirmed a band gap modulation of the $Be_xZn_{1-x}O$ films while maintaining a hexagonal crystal structure with a continuous shift in the peak position in XRD from hexagonal ZnO (34.31°) to hexagonal BeO (41.1°), and an optical band gap shift towards the deep UV regions (from 3.24 eV to over 4.62 eV with Be composition of $x = 0 - 0.51$). Grain growth of $Be_xZn_{1-x}O$ films on large-mismatched substrates, showed that the Be concentration in the films affects the distribution of grains in terms of orientation, size, and composition. In order to interpret the variation of grain growth kinetics in crystalline $Be_xZn_{1-x}O$ as a function of Be concentration, a modified Zener model that describes metallic Be particles driving a pinning effect on grain boundary mobility was employed. It is shown that grain boundary drag from Be pinning particles induces compositional fluctuation of Be in local areas, and smaller grain size formation. On the other hand, coalescence of Be pinning particles at grain boundaries, along with increased its volume fraction, gives rise to a re-enhancement of grain growth driving force. This leads to the formation of a coarse-grained array by development of particular grain boundary junctions. The grain boundary junctions also act as a channel for uniform distribution of Be composition in crystalline $Be_xZn_{1-x}O$ ternary films.

■ EXPERIMENTAL SECTION

Film growth. $Be_xZn_{1-x}O$ alloy ($0 \leq x \leq 0.77$) thin films of thickness ~ 200 nm were prepared on *c*- Al_2O_3 substrates in a partial pressure (P_{O2}) of 2×10^{-3} Torr at a growth temperature of 400°C using the radio-frequency (RF: 13.56 MHz) magnetron co-sputtering (base pressure: 1.2×10^{-8} Torr). In order to change the Be concentration in the films, the RF power to the Be metal target (3N) was adjusted from 0 to 80 W, while the RF power of the ZnO ceramic target (5N) was fixed at 100 W. Films were prepared with almost constant thickness by controlling the growth time under fixed conditions. Prior to film growth, both ZnO and Be targets were sputtered in the vacuum chamber using a RF power of 50 W in 30 min to remove target surface contaminants.

Characterizations. The structural and optical properties of the films were evaluated by X-ray diffraction (XRD; $\lambda = 1.5418$ Å) and UV-visible spectroscopy measurements. Tapping mode atomic force microscopy (AFM) measurement was used to observe the surface morphologies of the films. To determine the surface electronic structure and chemical state of the films as a

function of Be composition, X-ray photoelectron spectroscopy (XPS) was performed in ultra-high vacuum (UHV: base pressure, 3×10^{-11} mbar) using an Omicron SPHERA hemisphere analyzer and monochromatic Al K$_\alpha$ X-ray source (hν = 1486.6 eV). Photo-excited electrons from the film surfaces were collected using a takeoff angle of 90°. Surface charging during XPS measurements, resulting from the insulating nature of the samples was compensated for using a low energy electron flood gun (Omicron CN10). The binding energy (BE) scale was calibrated using the C 1s position (284.5 eV) and the overall energy resolution was 0.6 eV. Elemental composition ratios were extracted including the electron means free path correction and using Schofield cross sections.[49] Peaks were fitted using a Shirley background and Voigt (convolved Lorentzian-Gaussian) functions.

■ AUTHOR INFORMATION

Corresponding Author

*E-mail: c.f.mcconville@warwick.ac.uk

Present Address

§ Science Institute, University of Iceland, Dunhaga 3, IS-107 Reykjavik, Iceland

Notes

The authors declare no competing financial interests.

■ REFERENCES

(1) Long, H.; Fang, G.; Li, S.; Mo, X.; Wang, H.; Huang, H.; Jiang, Q.; Wang, J.; Zhao, X. *Elec. Dev. Lett., IEEE* **2011**, 32, 54.

(2) Chu, S.; Wang, G.; Zhou, W.; Lin, Y.; Chernyak, L.; Zhao, J.; Kong, J.; Li, L.; Ren, J.; Liu, J. *Nat. Nanotech.* **2011**, 6, 506.

(3) Heo, Y. W.; Kwon, Y. W.; Li, Y.; Pearton, S. J.; Norton, D. P.; *Appl. Phys. Lett.* **2004**, 84, 3474.

(4) Nakahara, K.; Akasaka, S.; Yuji, H.; Tamura, K.; Fujii, T.; Nishimoto, Y.; Takamizu, D.; Sasaki, A.; Tanabe, T.; Takasu, H.; Amaike, H.; Onuma, T.; Chichibu, S. F.; Tsukazaki, A.; Ohtomo, A.; Kawasaki, M. *Appl. Phys. Lett.* **2010**, 97, 013501.

(5) Ryu, Y. R.; Lee, T. S.; Lubguban, J. A.; White, H. W.; Kim, B. J.; Park, Y. S.; Youn, C. J. *Appl. Phys. Lett.* **2006**, 88, 241108.

(6) Tsukazaki, A.; Ohtomo, A.; Kita, T.; Ohno, Y.; Ohno, H.; Kawasaki, M. *Science* **2007**, 315, 1388.

(7) Tsukazaki, A.; Akasaka, S.; Nakahara, K.; Ohno, Y.; Ohno, H.; Maryenko, D.; Ohtomo, A.; Kawasaki, M. *Nat. Mater.* **2010**, 9, 889.

(8) King, P. D. C.; Veal, T. D.; Schleife, A. J.; P´erez, Z. niga; Martel, B.; Jefferson, P. H.; Fuchs, F.; Sanjos´e, V.M. noz; Bechstedt, F.; McConville, C. F.; *Phys. Rev. B*, **2009**, 79, 205205.

(9) Allen, M. W.; Swartz, C. H.; Myers, T. H.; Veal, T. D.; McConville, C. F.; Durbin, S. M. *Phys. Rev. B* **2010**, 81, 075211.

(10) Janotti, A.; Van de Walle, C. G. *Rep. Prog. Phys.* **2009**, 72, 126501.

(11) Service, R. F. *Science* **1997**, 276, 895.

(12) Ohtomo, A.; Kawasaki, M.; Koida, T.; Masubuchi, K.; Koinuma, H.; Sakurai, Y.; Yoshida, Y.; Yasuda, T.; Segawa, Y. *Appl. Phys. Lett.* **1998**, 72, 2466.

(13) Ryu, Y. R.; Lee, T. S.; Lubguban, J. A.; Corman, A. B.; White, H. W.; Leem, J. H.; Han, M. S.; Park, Y. S.; Youn, C. J.; Kim, W. J. *Appl. Phys. Lett.* **2006,** 88, 052103.

(14) Klingshirn, C.; Fallert, J.; Zhou, H.; Kalt, H. *Appl. Phys. Lett.* **2007,** 91, 126101.

(15) Yang, C.; Li, X. M.; Gu, Y. F.; Yu, W. D.; Gao, X. D.; Zhang, Y. W. *Appl. Phys. Lett.* **2008,** 93, 112114.

(16) Khoshman, J. M.; Ingram, D. C.; Kordesch, M. E. *Appl. Phys. Lett.* **2008**, 92, 091902.

(17) Kim, W. J.; Leem, J. H.; Han, M. S.; Park, I. W.; Ryu, Y. R.; Lee, T. S. *J. Appl. Phys.* **2006**, 99, 096104.

(18) Han, M. S.; Kim, J. H.; Jeong, T. S.; Park, J.; Youn, C. J.; Leem, J.; Ryu, Y. R. *J. Cryst. Growth* **2007**, 303, 506.

(19) Dong, L.; Alpay, S. P. *Phys. Rev. B* **2011,** 84, 035315.

(20) Gan, C. K.; Fan, X. F.; Kuo, J.-L. *Comp. Mater. Sci.* **2010,** 49, S29.

(21) Kim, I. W.; Lee, K. M. *Nanotechnology* **2008,** 19, 355709.

(22) Park, S. I.; Cho, T. S.; Doh, S. J.; Lee, J. L.; Jung, H. J. *Appl. Phys. Lett*. **2000,** 77, 349.

(23) Pankove, J. I.: *Optical Processes in Semiconductors*; Dover Publications Inc., 1971, 34-36.

(24) Meeder, A.; Marr´on, D. F.; Rumberg, A.; Lux-Steiner, M. C.; Chu, V.; Conde, J. P. *J. Appl. Phys.* **2002**, 92, 3016.

(25) Rai, R. C.; Guminiak, M.; Wilser, S.; Cai, B.; Nakarmi, M. L. *J. Appl. Phys.* **2012**, 111, 073511.

(26) Shi, H. L.; Duan, Y. *Eur. Phys. J.* B **2008,** 66, 439.

(27) Denton, A. R.; Ashcroft, N. W. *Phys. Rev. A* **1991,** 43, 3161.

(28) Chen, Y.; Washburn, J. *Phys. Rev. Lett.* **1996**, 77, 4046.

(29) Ohring, M.: *Materials Science of Thin Films*; Academic Press, **1992**, pp 213-219.

(30) Thompson, C. V.; Carel, R. *J. Mech. Phys. Solids* **1996**, 44, 657.

(31) Fan, X. F.; Zhu, Z.; Ong, Y.-S.; Lu, Y. M.; Shen, Z. X.; Kuo, J.-L. *Appl. Phys, Lett.* **2007,** 91, 121121.

(32) Dang, W.; Fu, Y.; Luo, J.; Flewitt, A.; Milne, W. *Superlattice Microst.* **2007**, 42, 89.

(33) Amor, S. B.; Jacquet, M.; Fioux, P.; Nardin, M. *Appl. Surf. Sci.* **2009**, 255, 5052.

(34) Allen, M. W.; Zemlyanov, D. Y.; Waterhouse, G. I. N.; Metson, J. B.; Veal, T. D.; McConville, C. F.; Durbin, S. M. *Appl. Phys. Letts.* **2011**, 98, 101906.

(35) Tay, Y. Y.; Li, S.; Sun, C. Q.; Chen, P. *Appl. Phys. Letts.* **2006**, 88, 173118.

(36) King, P. D. C.; Veal, T. D.; Payne, D. J.; Bourlange, A.; Egdell, R. G.; McConville, C. F. *Phys. Rev. Lett.* **2008**, 101, 116808.

(37) Linsmeier, C.; Wanner, J. *Surf. Sci.* **2000**, 454-456, 305.

(38) Wiltner, A.; Linsmeier, C. *New J. Phys.* **2006**, 8, 181.

(39) Linsmeier, C.; Wanner, J. *Surf. Sci.* **2000**, 454-456, 305.

(40) Woodruff, D. P.; Delchar, T. A.; *Modern Techniques of Surface Sciene,* 2nd edition, Cambridge University Press, **1944**, pp 2-4.

(41) Porter, D. A.; Eastering, K. E.; Sherif, M. Y.: *Phase Transformations in Metals and Alloys,* 3rd edition*:* CRC Press, **1984**, pp 143.

(42) Burke, J. E.; Turnbull, D. *Prog. Metal Phys.* **1952**, 3, 220.

(43) Zener, C. Trans. AIME **1948**, 175, 15.

(44) Ingham, B; Linklater, R.; Kemmitt, T. *J. Phys. Chem. C* **2011**, 115, 21034.

(45) Harper, J. M. E.; Cabral, J. C.; Andricacos, P. C.; Gignac, L.; Noyan, I. C.; Rodbell, K. P.; Hu, C. K. *J. Appl. Phys.* **1999**, 86, 2516.

(46) Hillert, M. *Acta Metallurgica* **1965**, 13, 227.

(47) Liu, W.-R.; Hsieh, W. F.; Hsu, C.-H.; Liang, K. S.; Chien, F. S.-S. *J. Appl. Cryst.,* **2007**, 40, 924.

(48) Hearne, S. M.; Trajkov, E.; Jamieson, D. N.; Butler, J. E.; Prawer, S. *J. Appl. Phys.,* **2006**, 99, 113703.

(49) Scofield, J. J. *Electron Spectrosc.* **1976**, 8, 129